Galindo, J.; Navarro, R.; Tarí, D.; Moya-Torres, F. (2021). Analysis of condensation and secondary flows at three-way junctions using optical visualization techniques and computational fluid dynamics. International Journal of Multiphase Flow. 141:1-15. https://doi.org/10.1016/j.ijmultiphaseflow.2021.103674

References

[1] J. Galindo, R. Navarro, D. Tari, F. Moya, Analysis of condensation and secondary flows at T-junctions using optical visualization techniques and Computational Fluid Dynamics, International Journal of Multiphase Flow (2021). doi:10.1016/j.ijmultiphaseflow.2021.103674.

Analysis of condensation and secondary flows at three-way junctions using optical visualization techniques and Computational Fluid Dynamics

J. Galindo[a], R. Navarro[a], D. Tarí[a], F. Moya[a,*]

[a] *CMT - Motores Térmicos, Universitat Politècnica de València*
Camino de Vera, 46022 Valencia

Abstract

Three-way junctions are employed in almost all piping systems, whenever two streams need to be merged into one duct. In some applications, the mixing between streams plays an important role for determining the performance of downstream elements. The situation is particularly interesting for low pressure Exhaust Gas Recirculation (EGR) junctions featured in piston engines, where warm humid exhaust gases meet cold fresh air, since the mixing of both streams can produce water condensation. This condensation deteriorates the integrity and performance of the adjacent compressor wheel. This work explores the aforementioned flow configuration in a three-way junction by means of a novel gas test bench that allows the characterization of the transversal section at the junction outlet, and 3D Computer Fluid Dynamics (CFD) simulations embedded with a previously-developed condensation model. Two optical techniques are employed: laser particle image velocimetry, which is used to characterize the cross-section secondary flows, and planar laser-induced visualization, which is employed for the first time to obtain the condensation pattern. The experimental measurements are conducted at two different working points and for two different three-way junction designs, being in agreement with 3D CFD simulations. Particularly, the overall luminosity captured in the experiments presents the same trends than the numerical condensed mass fraction. This innovative validation proves that a CFD model employing a psychrometric-based condensation submodel can be used as a tool to quantify the condensation produced in a three-way junction. The proposed tools are shown to be helpful for the development of advanced LP-EGR systems to reduce NO_X, CO_2 and particulate matter emissions during engine warm-ups.

Keywords:

Optical techniques, Three-way junction, In-flow Condensation, Mixing streams, Low-Pressure EGR

1. Introduction

Many industrial applications involve mixing processes, either between streams of different species or single-species flows but with different thermodynamic properties. Examples include power plants, in which hot and cold water is combined [1, 2], the mixture of different fluids in chemical processes or the different connections in internal combustion engines piping systems. This study aims at investigating the mixing of streams of humid air with different psychrometric conditions happening in a three-way junction. Given the broad scope of these processes, the boundary conditions have been particularized to that of Low-Pressure Exhaust Gas Recirculation (LP-EGR) junctions belonging to piston engines, in which EGR is mixed with fresh air.

Exhaust gas recirculation is a passive technique to reduce emissions that consists in reintroducing a fraction of the exhaust gases back into the engine cylinders. By doing this, the release of combustion energy is distributed into a higher amount

*Corresponding author. Tel.: +34 963 877 650
Email addresses: galindo@mot.upv.es (J. Galindo), ronagar1@mot.upv.es (R. Navarro), datade@mot.upv.es (D. Tarí), framoto1@mot.upv.es (F. Moya)

of gas, which reduces the maximum in-cylinder temperatures and therefore decreases NOx emissions [3]. For turbocharged engines, there are two main paths to reintroduce the EGR into the fresh air line (see Fig. 1): either taking the exhaust gases before the turbine to send them after the compressor or extracting the exhaust gases downstream the aftertreatment to reintroduce them before the compressor. The former is know as high-pressure EGR (HP-EGR) and the latter is called LP-EGR, since EGR is conducted in the high-pressure or low-pressure side of the engine, respectively.

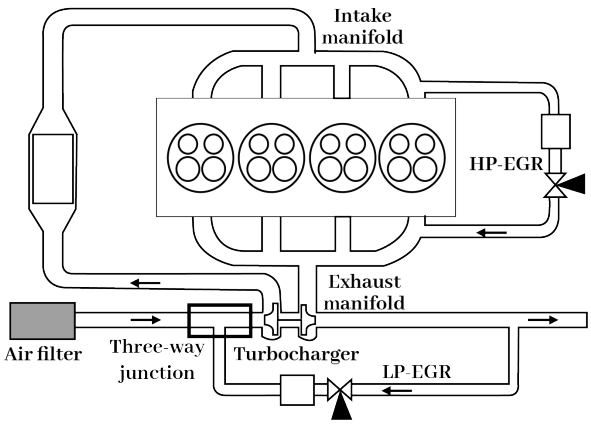

Figure 1: Layout of a turbocharged four cylinder internal combustion engine, featuring different EGR routes.

HP-EGR is well established in current automotive engines, but manufacturers are lately placing LP-EGR in the spotlight, due to its benefits when compared to HP-EGR. For instance, LP-EGR conducts the mixing between the exhaust gases and fresh air far upstream from the cylinders, which overcomes the issues of uneven EGR cylinder-to-cylinder distributions of HP-EGR [4, 5]. Furthermore, LP-EGR does not detract energy from the turbocharger as HP-EGR does, and allows using higher EGR rates than HP-EGR, which increases its benefits on emissions.

Unfortunately, a drawback appears when using EGR during the engine warm-up or at cold ambient conditions [6], since the water vapor of the exhaust gas may condense at the EGR cooler [7] and in the mixing region between fresh air and EGR stream [8]. This condensation may happen at HP-EGR [9] and LP-EGR alike [10], but it is especially harmful in the latter, since EGR is reintroduced before the compressor. In this way, the condensates may reach the compressor impeller (which is spinning at high speeds) in the form of droplets, damaging the blades [11]. Serrano et al. [12] performed an experimental study of the erosion of the impeller caused by the condensation produced on the LP-EGR system. This impact may produce, if prolonged over time, an important damage on the leading edges of the compressor which worsens its efficiency and poses a limit to its durability.

To study in-flow condensation problems, Serrano et al. [13] developed and verified a psychrometric-based model to calculate the water condensed at each cell of a 3D Computer Fluid Dynamics (CFD) case. Galindo et al. [14] shown that this model provided condensation mass flow rates that correlated well with compressor damage, by observing the eroded state of several impellers after 50-hour durability tests. Even though the model has been validated for assessing the risk of compressor wear depending on the operating conditions, the ability of such condensation model to predict accurate condensation distributions due to the mix of humid streams in junctions has not been assessed yet. Indeed, changes in the EGR rate or the junction design entail a modification in the cross section distribution of condensed water [15], which determines the compressor damage as it dictates the kinetic energy of the droplets impacting on the impeller blades, together with the compressor rotating speed.

Literature about flow phenomena in three-way junctions is extensive, particularly for 90° T-junctions [16, 17, 18]. Zhou et al. and Evrim et al. studied the thermal mixing in a T-junction [19, 20, 21] showing a range of experimental techniques to characterize such mixing, whereas Georgiou and Papalexandris [22] studied the same problem with CFD. In the framework of air and EGR mixing, Reihani et al. [23] experimentally characterized its impact on compressor performance and Sakowitz et al. [24] numerically analyzed the existing turbulent flow mechanisms. Unfortunately, none of them have studied the condensation phenomena in three-way junctions.

In this work, a novel flow test rig able to assess conden-

sation in three way junctions is developed, which provides hot humid air to one junction inlet and cold air to the other. Planar laser-induced visualization, which is used in the scope of multiphase problems in other works [25], is employed for the first time in this paper (to the authors' knowledge) to experimentally characterize condensation patterns in three-way junction. Besides, laser particle image velocimetry (PIV) measurements [26, 27] are also conducted to obtain secondary flows at the junction outlet cross-section. Notice that direct measurements of mixing condensation, that could be performed using separators to collect liquid water as presented by Chen et al. [28], are not valid for the studied problem as the technique will affect the flow mixing and thus the generated condensation. Concerning the numerical simulations, the commercial code STAR-CCM+ [29] is used to conduct the CFD campaign, featuring the previously mentioned condensation model [13]. The objective of this work is therefore to assess the sensitivity of condensation to changes in junction geometry and working conditions, both experimentally and numerically.

The experimental test bench is explained in Section 2, together with the different techniques used to characterize the flow distribution and condensation at the junction outlet. Next, the numerical configuration is presented in section 3. The results are shown and discussed in Section 4, comparing 3D-CFD simulations with PIV measurements and planar laser-induced images. An example of the potential of the proposed multiphase 3D CFD configuration for improving LP-EGR systems is provided in Section 5. Finally, the conclusions obtained are exposed in Section 6.

2. Experimental apparatus

This work presents an experimental campaign conducted in a continuous flow test rig. The test bench is equipped with optical accesses in order to use PIV and planar laser-induced visualization at the outlet cross section of the geometry. In this section, the test facility and the employed visualization techniques are described.

2.1. Condensation test bench

In order to assess the condensation produced in LP-EGR junctions (as the one framed in Fig. 1), a novel test bench has been developed, which provides hot humid air through one branch (representing EGR) and conditioned air through the other (to simulate ambient intake from cold climates). The pair of inlets of the three-way junction are fed by their corresponding branch, while the outlet directly blows into the test rig (free discharge configuration). A free discharge is more convenient for the sake of outlet visualization, and section 3.1 will show that the impact of removing the outlet duct is small. For LP-EGR applications, a compressor would be installed in that outlet duct. However, Galindo et al. [15] concluded that the presence of the compressor has a low influence on the formation of condensation; the error being 4% or lower for representative LP-EGR boundary conditions.

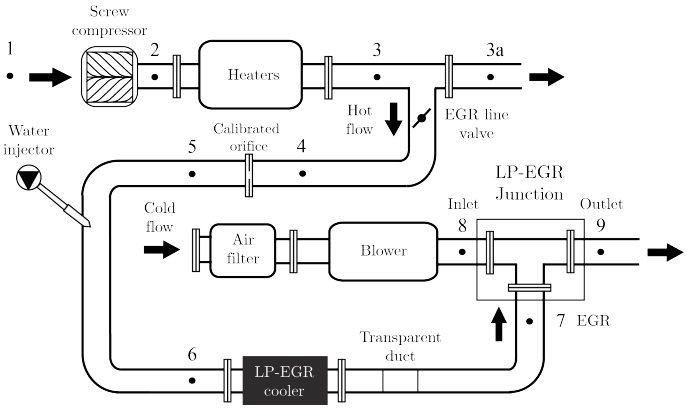

Figure 2: Layout of the condensation test bench

Figure 2 depicts the layout of the test rig employed. The objective of the test rig is to provide the three-way junction geometry with hot humid flow (station 7) and cold flow (station 8). Regarding the hot humid flow stream (EGR), the method proposed by Galindo et al. [30] is followed. In this way, at the core of the rig (between stations 1 and 3), there is a volumetric screw compressor (Atlas Copco ZE 3C-300-5E VSD) that supplies compressed air and five heaters (9kW each) that increase the flow temperature up to 400°C for the sake of enhancing subsequent injected water evaporation. A counter-pressure valve controls the mass flow rate (MFR) that goes through the

Table 1: Instrumentation range and accuracy[1]

Sensor	Variable	Range	Accuracy [%]
K-type thermocouples	Temperature	-260 – 1260 °C	1
Pressure sensor	Pressure	0 – 6 bar	0.3
Flow meter	Air mass flow	0 – 720 kg/h	1
Weighing scale	Water injected mass	0 – 20 kg	0.1

[1] According to datasheets

three-way junction EGR inlet. A calibrated orifice (located between stations 4 and 5) was used to set the desired MFR in the EGR line, by previously determining the relation between orifice pressure drop and the MFR. To simulate humid LP-EGR flow conditions, water is injected between stations 5 and 6 to increase the specific humidity up to the desire value with a Bosch AdBlue dosing module denoxtronic 2.1 injector controlled by an Arduino board, able to inject a maximum of 3 l/h. Full evaporation is guaranteed by the aforementioned high flow temperature and 3 meters of pipe downstream the injection. Once the water is evaporated, the flow temperature is reduced in the LP-EGR cooler down to the target value at station 7, being higher than the dew point. To make sure that no water exists at the LP-EGR cooler outlet, a transparent duct is installed there (see Fig. 2). To produce the stream of cold air, air is cooled and dried in a climatic chamber. Then, using a blower, it is pushed through the cold branch to be mixed with the humid stream in the LP-EGR junction (stations 7-9).

The operating range and accuracy of the instrumentation used to establish the working point is shown in Table 1. K-type thermocouples are used for measuring temperature in the test rig. Piezoresistive pressure sensors are mounted along the different ducts. Both temperature and pressure measurements are obtained at all stations (1-9) in Fig. 2. A flow meter is installed in the cold flow branch downstream of the blower, together with a frequency controller to set the desired air mass flow rate. A weighing scale was employed in the test rig to double-check the water injection rate. An acquisition frequency of 2 Hz was used on every sensor.

2.2. *Laser PIV measurements*

In this work a PIV campaign is conducted to characterize the flow distribution in a cross-section just downstream the junction discharge. Fig. 3 shows a schematic representation of the laser PIV system. In this study, a standard 2D PIV system by TSI has been selected to measure 2D instantaneous velocity fields following the validated methodology presented by Torregrosa et al. [31] and Pastor et al. [32]. This involves a 15 Hz flashlamp pumped Nd:YAG laser with 135 mJ/pulse at 532 nm. A redirecting optical system with a set of lenses and mirrors is used to set the measurement plane a 4 megapixel, 12-bit straddle CCD camera (PowerView Plus 4MP) and a synchronization device is used to capture the images. Tests were carried out with both fresh air and EGR inlets seeded with particles to allow the processing of the velocimetry. For this purpose, oil droplets of 1 μm of diameter are supplied to the flow using an atomizer. A commercial synthetic oil based on liquid paraffin and isopropyl palmitate is employed, in accordance with the work of Torregrosa et al. [31].

Images were processed with the software TSI Insight 3G in order to obtain the components of the velocity vectors and the in-plane velocity modules. The software is configured to obtain the maximum available spatial resolution of velocity vectors. Additional custom routines are developed in Python to crop the outlet section of the raw snapshot (Fig.4a) and for representing velocity vectors and contours previously calculated by the software TSI Insight 3G.

Figure 4a depicts a raw cross section snapshot, detailing the available region of interest (ROI) of the cross section where the

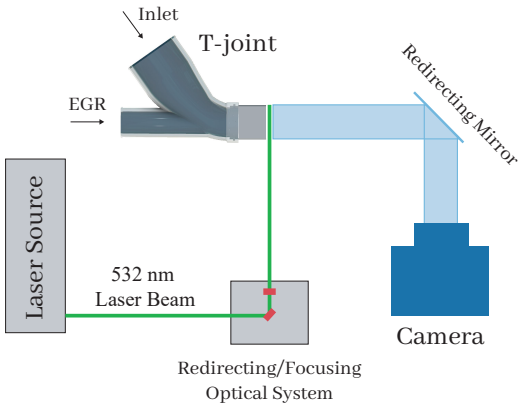

Figure 3: Schematic representation of the employed laser PIV apparatus.

velocity is calculated (shown in Fig. 8). Figure 4b shows an example of the postprocessing performed in the measurement plane.

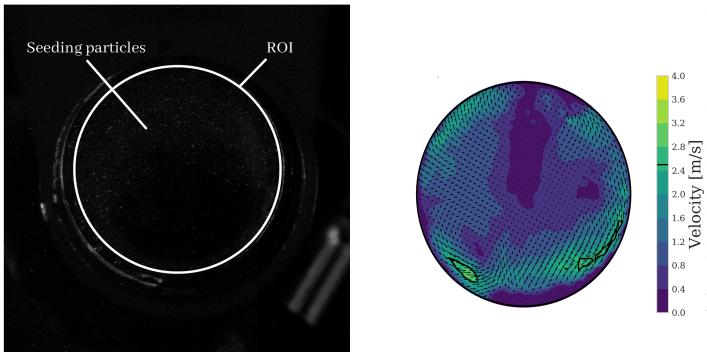

(a) Raw snapshot. (b) Postprocessed velocity field.

Figure 4: Example of laser PIV process to measure velocity field at the three-way junction outlet.

The magnification of the images was 860 pixel/mm, whereas the visualization resolution and the size of the cross correlation were set to 16x16 pixels so as to prevent an excessive interpolation during data processing. The time elapsed between the two laser shots was established as 15 μs, since it provided the flow velocity field in the greatest detail. This is the maximum time difference with which the particles at the two snapshots are confined within the laser sheet. Velocity vector field is averaged by considering 200 images for each case, which extend over a time period of 3 ms. If the uncertainty of time-averaged in-plane velocity [33] is spatially averaged for the cross section of interest and normalized with the mean in-plane velocity (temporally and spatially averaged) in accordance with Eq. 1, normalized uncertainties $\widetilde{U_u}$ between 10% and 11% are obtained for the cases considered in Section 4.3.

$$\widetilde{U_u}(\%) = \frac{\widetilde{\sigma_{\bar{u}}}/\sqrt{N}}{\hat{\bar{u}}} 100 \quad (1)$$

2.3. Planar laser-induced visualization

Considering the impossibility of providing an accurate quantitative measurement of the liquid phase distribution in a foggy environment, the condensation pattern is assessed by means of planar laser-induced visualization in this work. Given the difficulty of quantifying the uncertainty of liquid sprays visualization [34], the main objective is therefore to characterize experimentally the locus at which condensation is produced. To allow a proper comparison of the qualitative changes in condensation distribution, the same luminosity conditions have been kept for all cases. In any case, the differences in the local amount of condensed water should produce a corresponding variation in the luminosity distribution. This effect will be used in Section 4.4 in order to compare the condensates predicted by CFD simulations with the laser-induced visualization of the condensation pattern.

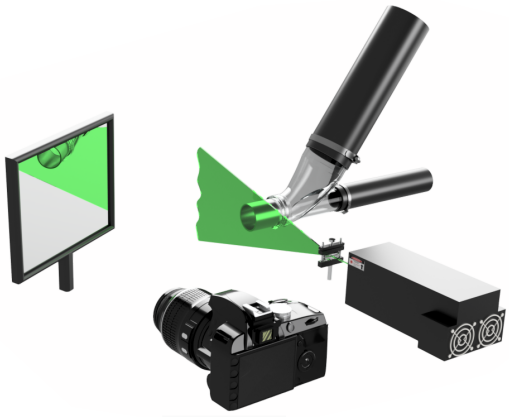

Figure 5: Schematic representation of the employed planar laser-induced visualization apparatus.

The layout for the laser-induced visualization (Fig. 5) may seem similar to that of the PIV measurements depicted by Fig.3, but the laser and camera are different. The measurements conducted with the planar laser-induced visualization involve a 3

kW laser with a wavelength of 532 nm (MGL-N-532B 3kW) provided by a power supply (PSU-H-LED) and a plano-concave lens for the laser beam expansion to cover the diameter of the circular outlet section with around 1 mm thickness at the measurement section. A 24 megapixel, DSLR camera (Nikon D3400) and a redirecting mirror to protect the equipment from the condensed water are used to take the pictures. A long exposition of 3 seconds is employed to average the temporal fluctuations of the condensation pattern.

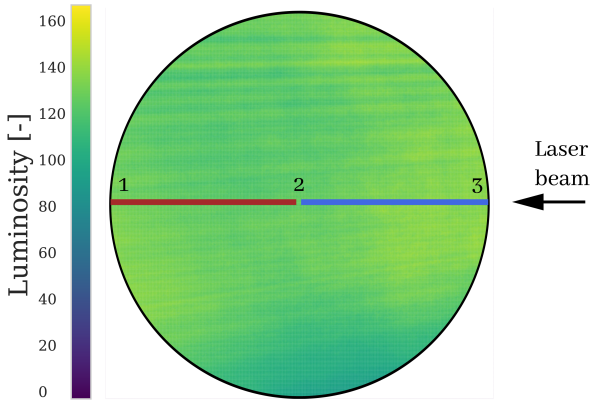

(a) Luminosity distribution for a homogeneous cloud of dopant.

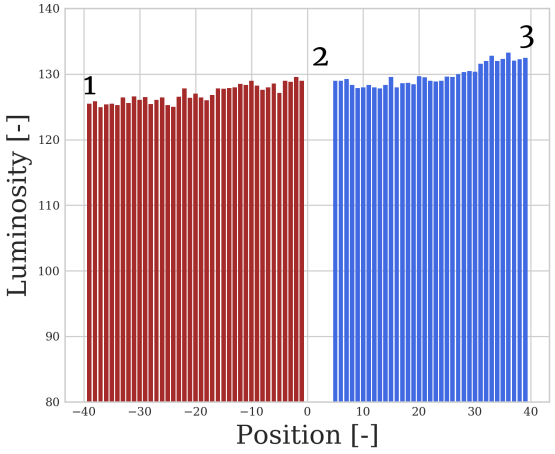

(b) Luminosity profile reduction in the direction of horizontal lines 3 to 2 (blue line) and 2 to 1 (red line) of Fig. 6a.

Due to the plano-concave lens, a correction of the measured luminosity data is required. Figure 2.3 shows a picture of the measured luminosity for a still ambient with a cloud of droplets of 1 μm diameter obtained by means of an oil atomizer. An ideal laser beam would produce a homogeneous sheet in these conditions. However, Fig. 6a presents a luminosity loss due to the beam expansion, quantified at two lines in Fig. 6b. Therefore, the uneven distribution shown in Fig. 6a is characterized and employed to correct the raw pictures that will be obtained in the experimental campaign discussed in section 4.1. The correction procedure is done by virtue of equations 2 and 3, in accordance with the works of Pastor et al. [35] and Charogianni [36]:

$$f_L(i) = \frac{L_{max}}{L_i} \tag{2}$$

$$L_{corr}(i) = f_L(i) L_{raw}(i) \tag{3}$$

Figure 7 shows, at the top left side, a sample of raw data extracted directly from the tests, together with the reference laser sheet characterization (bottom left) within the region of interest (ROI). The two pictures are then processed to depict the measured luminosity. The laser sheet reference luminosity (bottom center) is employed to calculate the distribution of the correction factor (Eqn. 2), by dividing the maximum luminosity of the reference sheet by the luminosity of each pixel of the reference sheet. Finally, the luminosity of the considered test (top center) is corrected by means of equation 3 to obtain the processed image on the right side of Fig. 7.

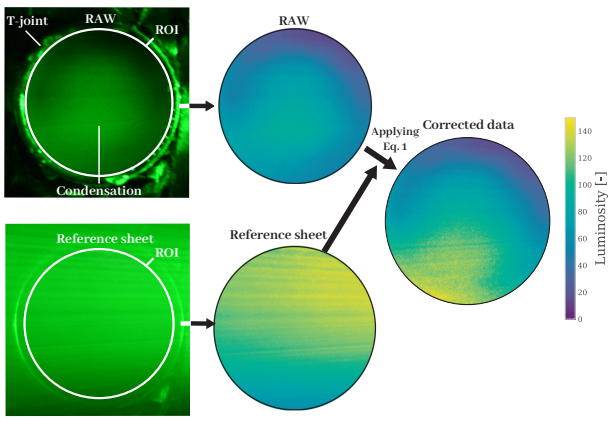

Figure 7: Method to correct the raw data measured with the planar laser-induced visualization.

3. Numerical configuration

3.1. Geometry and mesh

As aforementioned, the element studied in this work is a three-way junction, such as the one shown in Fig. 8. In particular, the junction has two entries, one for the cold fresh air (inlet) and one for the humid and warm flow (EGR). The lengths of the inlet and the EGR lines in the numerical domain are extended three additional diameters upstream from the actual junction entries (see Fig. 12). These extrusions are employed to limit the impact of the boundary conditions in the region of interest. A sensitivity study about extruded ducts at both inlets was performed. When no extrusions are employed, the condensation mass flow rate at the studied cross section changes by 5%, comparing with the baseline case with three-diameter extrusions. If the extrusions are doubled in length, a difference of only 0.7% appears. Balancing computational cost and impact of boundary location on the solution, the extrusions of three diameters are therefore selected.

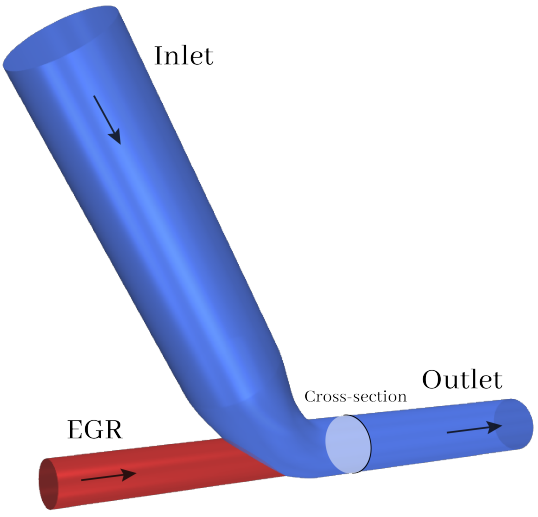

Figure 8: Geometry of the LP-EGR junction in the CFD model.

Notice how the compressor that should be in the outlet duct of a LP-EGR junction system is not considered neither in the measurements nor in the simulations, for the reasons discussed in section 2.1. In the experiments (see Fig. 2), the three-way junction discharges directly into the test rig, whereas the CFD domain features a five-diameter duct downstream the original outlet cross-section (see Fig. 8), again for limiting the impact of boundary location in the region of interest.

To assess the impact of neglecting the actual experimental configuration in terms of outlet discharge, a more representative domain is considered in Fig. 9b. In this case, there is free flow discharge from the junction outlet into a cylindrical volume of 5 outlet diameters. The difference in condensation between the free-discharge domain (Fig. 9b) and the extruded-duct configuration 9a at the reference cross section is below 3%, considering that the target surface is 2 mm away from the duct outlet, since there is where visualization techniques are conducted. This difference in condensation is due to the expansion of the discharge stream after being released from the duct over these 2 mm. Figure 10 shows a comparison between the lower part of the target cross section with both domains. For the free-discharge domain (bottom side of Fig. 10), a small fraction of condensation region exists outside the target surface (depicted as a white line), which accounts for this missing 3% of condensation compared to the extruded-outlet domain (top side of Fig. 10) with the same cross-section area. Since the computational effort of the case representing the free discharge was 2 times higher than that of the extruded outlet duct, it was decided to proceed with the latter for the rest of the work.

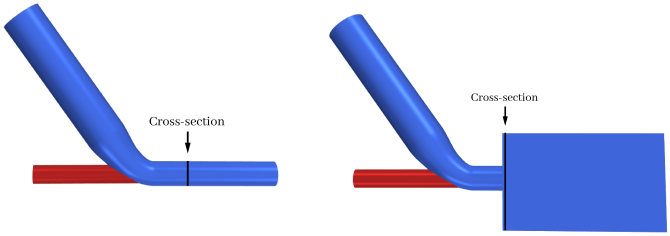

(a) Extruded-outlet domain. (b) Free-discharge domain.

Figure 9: Comparison between the domains simulated, (a) the selected domain with the extruded outlet and (b) the free-discharge domain

The meshing strategy corresponds to the approach proposed by Galindo et al. [15]. The meshed domain is depicted in Fig. 11. A polyhedral grid is employed for the region of interest. A structured mesh is generated in the extruded regions of both inlet and EGR lines. Prism layers are created on the

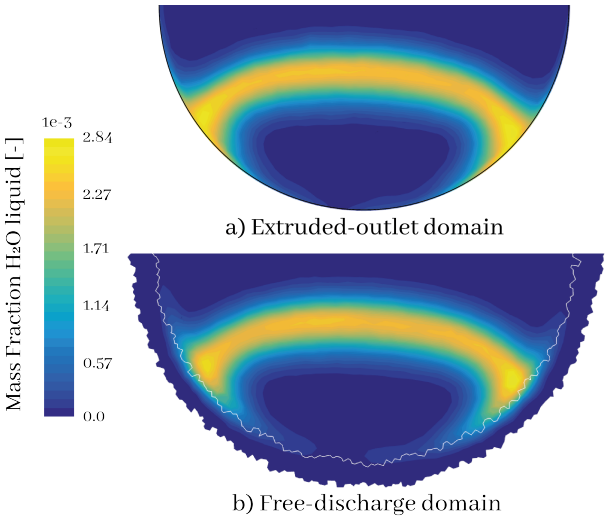

Figure 10: Contours of condensed mass fraction at the bottom part of target cross-section with same area for (a) the extruded outlet domain and (b) the free-discharged domain.

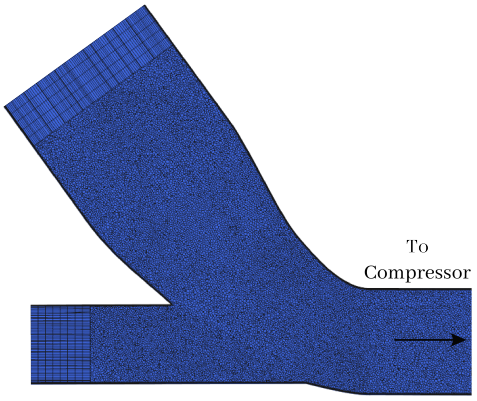

Figure 11: Longitudinal cross section of the 11 million cells mesh for LP-EGR junction. The extruded ducts are not shown entirely.

walls, which improve the flow resolution on the velocity boundary layer.

A grid independence study is conducted with three meshes of different number of cells: 300 thousand, 3 million and 11 million cells. A representative parameter of the physical problem considered in this work was selected to address the mesh independence study, i.e., the mass flow rate of condensed water going through the target cross section, corresponding to the compressor inducer. While the refinement from 300k to 3M cells entailed a difference of 13% in the prediction of condensates at the T-junction 12b, a subsequent increase of mesh density modified the condensation mass flow rate only by 1%. Then, the 3 million cell mesh was selected for conducting the rest of the work. The employed grid features a base size of 0.6 mm, with 99% of its wall cells presenting a y^+ value below 1.

3.2. Setup and boundary conditions

The numerical configuration of the simulations is set up following in accordance with the work of Galindo et al. [14, 15]. The segregated solver is selected in the 3D-CFD Finite Volume Method code STAR-CCM+ [29], employing second-order upwind schemes for the discretization of convective terms. Even though the maximum Mach number does not go above 0.2 for the considered simulations, the flow is not regarded as incompressible and the ideal gas equation of state is employed for air and vapor water.

For modeling turbulence (which is required as Reynolds numbers based on inlet and EGR diameters range between $18 \cdot 10^3$ and $51 \cdot 10^3$), RANS and unsteady RANS (URANS) approaches were used, both employing the k-ω SST submodel [37]. Steady RANS simulations have been used for the geometry shown in Fig. 12a, whose reduced mixing produced a fluctuation of condensation MFR (once converged) of less than 1%. However, URANS was required with the geometry depicted in Fig. 12b due to the strong condensation instability produced by the detachments that will be discussed in section 4.2. A time-step size of $1 \cdot 10^{-4}$ s and a second-order implicit unsteady solver were considered when transient simulations were required, following the methodology presented by Galindo et al. [14]. For these unsteady simulations, time-averaged values are obtained once the solution is stable by averaging over additional 400 time steps (40 ms).

Concerning the boundary conditions, mass flow rate is established in both fresh air and EGR inlet boundaries, together with the total temperature and the mass fraction of each component (dry air and water vapor). The corresponding values for the two studied working conditions will be presented in Table 3. Turbulence intensity of 0.01 was set in both inlet boundaries. Regarding the outlet specifications, the test rig ambient pres-

sure is established as the outlet boundary condition, whereas the compressor intake in an internal combustion engine would operate slightly below atmospheric pressure. In any case, Tarí [38] showed a low impact of the junction pressure on the generated condensation rate.

The condensation submodel implemented in STAR-CCM+ is based on the work presented by Serrano et al. [13], which estimates the quantity of condensates that a given cell of the simulation geometry should produce in order to reach an equilibrium state at saturated conditions, following an isenthalpic process. The estimation of the vapor that condenses is calculated with the psychrometric variables of the gas (temperature, pressure and specific humidity), which are in turn calculated employing Dalton's Law and an Antoine equation for the saturation curve. Then, the model interacts with the numerical solver through the transport equation source terms, replicating the actual condensation process. Notice that droplet nucleation and subsequent Lagrangian particle tracking, as employed by Schuster et al. [39, 40] or Wittmann et al. [41] in the framework of condensation in radial turbines, are not considered in this work due to the significant increase in computational effort when shifting to a Eulerian-Lagrangian approach [42].

A general transport equation is presented in Eq. 4. The solved transport equations governing the flow field (save for k and ω turbulent transport equations) are yielded when the terms in Table 2 are particularized in Eq. 4, considering that diffusion coefficients are *effective* (RANS). Besides, the custom source terms of mass, energy and momentum due to the condensation submodel are presented in Eqs. 5, 6 and 7 respectively.

$$\frac{\partial(\rho\varphi)}{\partial t} + \nabla\left(\rho\varphi u_i\right) = \nabla\left(\rho\Gamma_\varphi \nabla(\varphi)\right) + S_\varphi \tag{4}$$

$$S_{vap} = \frac{\rho\gamma_{air}(w_f - w_1)}{\Delta t} \tag{5}$$

$$S_{ener.} = -S_{vap}(L - c_p T) \tag{6}$$

$$S_{mom..} = S_{vap}\overrightarrow{u} \tag{7}$$

Table 2: Convective, diffusive and source terms of solved transport equations (excluding turbulence).

Equation	φ	Γ_φ	S_φ
Mass	1	–	S_{vap}
Species	y	D	S_{vap}
Momentum	u_i	ν	$-\partial p/\partial x_i + f_m + f_v + S_{mom}$
Energy	h	α	$-Dp/Dt + f_t + f_v + S_{\text{ener}}$

The main simplifications and hypotheses assumed for the model implementation are:

- Instantaneous condensation: since low velocities appear at the LP-EGR junction, it is acceptable to assume that condensation occurs instantaneously whenever a cell presents oversaturation. In this way, growth rate of water droplets is not modeled [43]. This hypothesis may not be appropriate in applications where condensation takes place in high velocity flow fields, such as in steam turbines or rocket engines.
- Condensed liquid water is not modeled. Liquid water mass fraction is low, even with highly condensing boundary conditions. Therefore, the impact of this simplification on the conservation of the transport variables is negligible.

More information about the underlying hypotheses of the condensation submodel can be found in the work of Serrano et al. [13].

4. Results and discussion

First, the different operating conditions and geometries assessed in the test bench and in the CFD simulations are presented in section 4.1. Then, the flow longitudinal evolution is presented only for the CFD simulations, since it is not feasible to be obtained by means of experimental measurements. Afterwards, the comparisons between PIV measurements and CFD predictions of cross-section in-plane velocity field are shown in

section 4.3. Finally, the condensation patterns calculated using CFD are compared with the corresponding planar laser-induced visualizations in section 4.4.

Comparing the resolutions of the data acquisition for each technique at the junction outlet cross section: 1806 values of velocity vectors are obtained for PIV measurements with the configuration and image processing described in Section 2.2, 4140 faces are available with the mesh employed in the CFD simulations (see Section 3.1) for displaying velocity and water mass fraction contours, and for the Planar laser induced visualization about 1 megapixel are extracted from the raw images obtained with the setup presented in Section 2.3.

4.1. Test campaign

Table 3: Studied operating points.

Operating points	P1	P2
EGR Temperature [°C]	50	50
EGR mass flow rate [kg/h]	40	40
Specific Humidity [g/kg]	60	60
Inlet Temperature [°C]	-2	0
EGR rate [%]	21	32
Inlet mass flow [kg/h]	150	85

As mentioned in section 1, the purpose of this work is to analyze the secondary flows and the condensation at the outlet of a three-way junction, evaluating the agreement between experimental optical techniques and CFD simulations. To reduce the danger of drawing case-specific conclusions, two operating conditions and two geometries are assessed. As can be seen in Table 3, the operating conditions considered in the test matrix present a 50% difference in the EGR rate (defined by Eq. 8), which is obtained by modifying the air inlet MFR. These operating points share the same EGR temperature, EGR mass flow rate, specific humidity and they have a similar inlet temperature. Galindo et al. [30] studied the range in which variables like EGR mass flow rate, specific humidity, etc. worked in a vehicle for a WLTP cycle. Values considered in Table 3 have been defined taking into account these working ranges.

$$EGR_{\text{rate}} = \frac{\dot{m}_{\text{EGR}}}{\dot{m}_{\text{EGR}} + \dot{m}_{\text{Air}}} \tag{8}$$

Additionally, two three-way junction geometries (Fig. 12) are used to study their influence on the condensation produced, with the objective of producing a completely different flow pattern and condensation. As can be seen, Fig. 12a shows a geometry where the EGR duct is aligned with the outlet duct. On the contrary, Fig. 12b depicts a geometry with the EGR branch oriented towards the fresh air inlet.

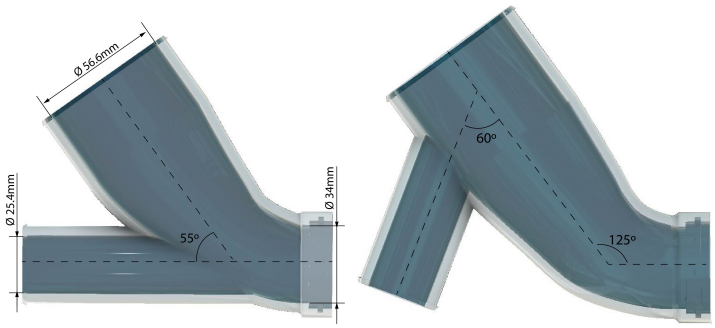

(a) Three-way junction A (b) Three-way junction B

Figure 12: Longitudinal slice and main dimensions of three-way junctions analyzed.

To assess the influence of different EGR rates and geometries, all two operating points and two geometries are tested (and measured with both laser techniques) and simulated with the 3D-CFD code at the cross-section showed in Fig 8, which is in the corresponding position at which the compressor impeller should be located.

4.2. Longitudinal evolution of the flow

In Figures 13 and 14, a longitudinal cross-section of the CFD simulation results is provided for the working point P1 (see Table 3) with both geometries of study. In the case of Fig. 14, the variables of the unsteady simulation are time-averaged. In these figures, the liquid condensation water produced by the CFD simulation at the junction due to the mixing process is shown. The three-way junction of Fig. 13 displays a reduced air-EGR mixing in the longitudinal section, due to the alignment between the EGR duct and the main duct. On the con-

trary, Fig. 14 shows a strong separation when the EGR stream is discharged into the air mass flow due to the geometry of junction B, which presents the EGR duct oriented slightly opposed to the main stream. The enhanced mixing at the longitudinal cross-section of junction B (Fig. 14) compared to junction A (Fig. 13) entails an increase in condensation, as will be seen in Section 4.4.

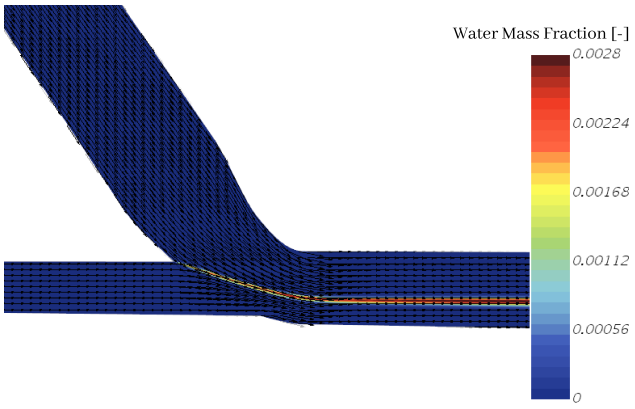

Figure 13: Condensation water mass fraction together with in-plane velocity vectors in the longitudinal section for the junction A at the operating point P1

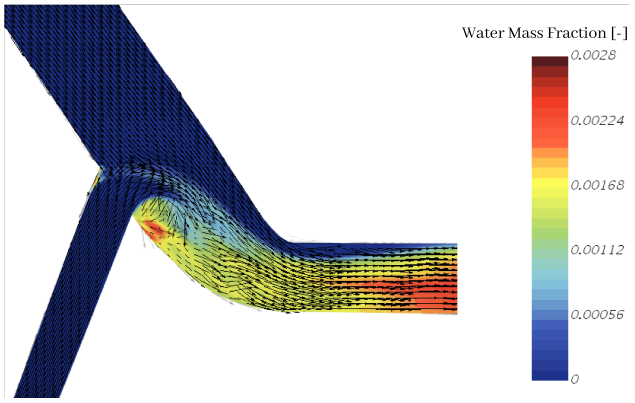

Figure 14: Time-averaged condensation water mass fraction together with in-plane velocity vectors in the longitudinal section for the junction B at the operating point P1

4.3. Transversal secondary flows: PIV vs CFD

According to Galindo et al. [15], the condensation produced in the junction depends on the intensity of the air-EGR mixing. Therefore, the first comparison to be conducted between experimental PIV measurements (as described in Section 2.2) and CFD simulations is in terms of secondary flows at the cross section of study (see Fig. 8). With this purpose, in-plane velocity contours of both techniques are shown in the Figs. 15, 16, 17 and 18 along with velocity vectors.

For all the figures, the iso-velocity of 2 m/s is represented at each figure, including as well dashed curved arrows to represent the main vortices that can be identified. In first place, Figures 15 and 16 show the velocity at operating points P1 and P2 while the three-way junction A is set. The flow at these working points is alike. There is a pair of large counter-rotating vortices in the upper part of the cross-section generated by the cold stream that comes from the upper duct, since this branch behaves as an elbow (see Fig. 13), thus creating the so-called Dean vortices [24, 44]. Such Dean vortices appear at curved pipes due to the inertia of the core stream, that tends to flow towards the outer part of the bend. This centripetal motion in the elbow plane is balanced by the fluid returning close to the walls [45]. Hence, a pattern of secondary flows is established as a pair of counter-rotating vortices [46]. These Dean vortices induce in turn a second pair of counter-rotating vortices in the lower part of the transversal section, because the EGR stream is aligned with the outlet pipe in three-way junction A (Fig. 13) and therefore is not suitable to create secondary flows by itself.

For the low mass flow rate case (P1), two small counter-rotating swirling structures are indeed created at the low part of the cross section in the CFD case (Fig. 15b), while the experimental case shows only one of the two swirl structures (Fig. 15a), probably due to their low intensity. Concerning the working point P2 with a higher mass flow rate than P1, Figure 16 shows the two pairs of counter-rotating swirling structures, both measured by PIV and predicted by CFD simulations.

Finally, Figures 17 and 18 show the results with the junction B, in which a higher penetration of the EGR stream exists due to the geometry. As a consequence, the presented vortical patterns and secondary flows are of greater intensity when compared to junction A (Figures 15 and 16). The impact of junction geometry is well predicted by CFD simulations.

The significant detachment of the EGR stream at junction B

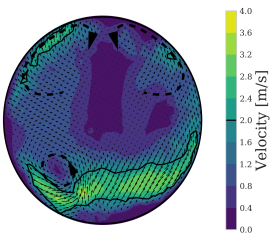

(a) PIV technique

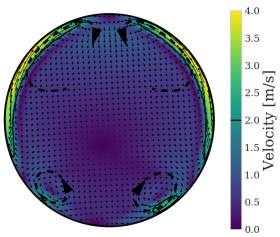

(b) CFD simulation

Figure 15: Comparison between the in-plane velocity field at P1 and junction A for the PIV technique (a) and the CFD RANS simulations (b). Large dashed arrows are manually added to highlight main vortical patterns.

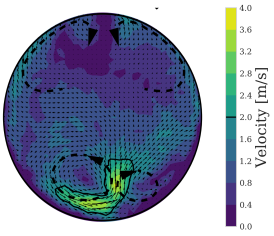

(a) PIV technique

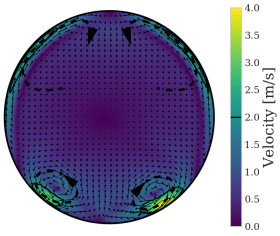

(b) CFD simulation

Figure 16: Comparison between the in-plane velocity field at P2 and junction A for the PIV technique (a) and the CFD RANS simulations (b). Large dashed arrows are manually added to highlight main vortical patterns.

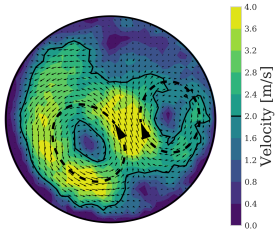

(a) PIV technique

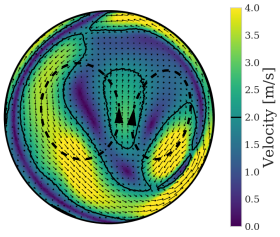

(b) CFD simulation

Figure 17: Comparison between the time-averaged in-plane velocity field at P1 and junction B for the PIV technique (a) and the CFD URANS simulations (b). Large dashed arrows are manually added to highlight main vortical patterns.

due its high penetration into the core stream and the sharp bend between its duct and the main duct (see Fig. 14), causes the flow of junction B to be inherently unsteady and thus require URANS instead of RANS, unlike junction A. These transient oscillations in junctions were also experienced by Lu et al. [1],

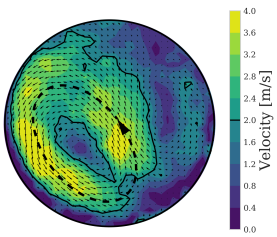

(a) PIV technique

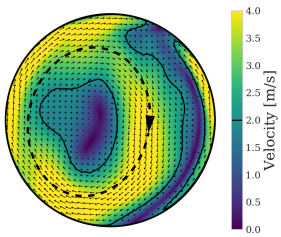

(b) CFD simulation

Figure 18: Comparison between the time-averaged in-plane velocity field at P2 and junction B for the PIV technique (a) and the CFD URANS simulations (b). Large dashed arrows are manually added to highlight main vortical patterns.

in the form of low-frequency temperature fluctuations due to the mixing of hot and cold streams. Lyne [47] first discovered that the elbow centrifugal pattern (and therefore the direction of the Dean vortex pair) can be reversed when shifting from steady to unsteady flow. Tunstall et al. [44] analyzed the complex vortical pattern at T-junctions, showing how the Dean vortices present an unsteady switch between different modes. Sakowitz et al. [24] found that Dean-like vortices were predicted with opposite directions depending on whether LES or k-ϵ URANS were considered.

The literature shows that flow separation makes the case to be more sensitive to variations of geometry and working points, and therefore it is more difficult to accurately predict its transversal secondary flows. One may have expected the Dean-like vortical pattern of the upper part of junction A (Figs. 15 and 16) to appear in junction B again, as the main duct bend angle is the same for both junctions. Aside from the reported complexity of the unsteady vortical phenomena, the greater intensity of secondary flows at junction B would mask any lesser pattern, such as the Dean vortices of junction A. The comparison of secondary flows strength can be assessed through the area determined by the iso-velocity of 2 m/s, being much greater at junction B (Figs. 17 and 18) than at junction A (Figs. 15 and 16).

All in all, there is an agreement between CFD simulations and the PIV technique at the Fig. 17, when observing the velocity pattern produced by the two counter-rotating swirling struc-

tures at the center of the cross section. These larger and more intense vortices increase the mixing of air and EGR streams compared to that of junction A. Working point P2 presents an EGR rate 50% greater than that of P1 (see Table 3), so the penetration of the EGR stream into the fresh air is even more intense than the one depicted in Fig. 14. This severe flow detachment at P2 for junction B generates a clearly asymmetrical in-plane velocity field in Fig. 18, in which both PIV and CFD depict a single large vortex, but with different rotating direction. As aforementioned, this unstable flow field is more challenging to be modeled by CFD due to its greater sensitivity to slight variations on geometry or upstream boundary conditions.

4.4. Planar Laser-induced Visualization vs CFD

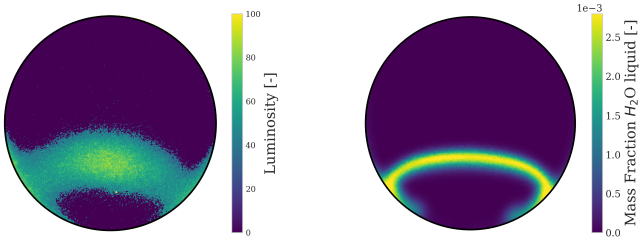

(a) Laser visualization (b) CFD simulation

Figure 19: Comparison between the luminosity on the Laser visualization (a) and the mass fraction of condensed water predicted by the CFD RANS simulation (b) at the outlet cross section of junction A for working point P1.

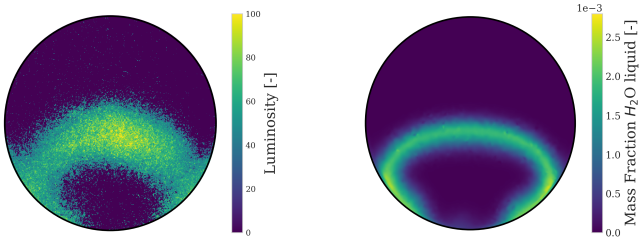

(a) Laser visualization (b) CFD simulation

Figure 20: Comparison between the luminosity on the Laser visualization (a) and the mass fraction of condensed water predicted by the CFD RANS simulation (b) at the outlet cross section of junction A for working point P2.

Section 4.3 has shown an overall good agreement between CFD simulations and experimental tests in terms of secondary flow patterns, which is critical for condensation [15]. In any case, the prediction of the condensation distribution at the target cross section is assessed by comparing the water mass fraction calculated by CFD simulations with the luminosity obtained by the planar laser-induced visualization described in Section 2.3. The underlying idea is that the condensation produced experimentally at the section is correlated with the measured luminosity, i.e, a greater quantity of condensed water would reflect light in a more intense way when a laser sheet is projected onto the cross section.

Figures 19, 20, 21 and 22 show the luminosity with a range between 0-255 for the case of the experimental laser visualization and the mass fraction of condensed water for the CFD simulations, depending on the working point and the geometry employed. The mass fraction of condensed water at CFD simulations as shown in these figures is obtained by calculating the condensed mass flow rate at the cross section and dividing by the total mass flow rate

Figures 19 and 20 show that the condensation is produced at the thin interface of the two streams (EGR and fresh air). As it is shown in Figures 15 and 16, the mixing occurs at the bottom part of the cross section due to vertices that add fresh air from the core to the lower side, which is dominated by the EGR stream. If junction A is kept but the EGR rate is increased (P2), Fig. 20 presents a higher penetration due to the higher EGR rate than Fig. 19. This difference causes a larger condensation interface due to the increase of air-EGR of mixing.

When three-way junction B is considered, Figures 21 and 22 show condensation at the whole perpendicular cross-section for both working points. This happens due to the stronger secondary flows and mixing existing for junction B, as seen previously in Figs. 17 and 18.

Finally, a quantitative comparison is conducted to assess the capability of the CFD model to predict the influence of junction geometry and working point on condensation. To do so, values of luminosity (experimental) and condensed mass fraction (numerical) depicted at Figs. 19-22 are averaged at the outlet cross section. The results for junction *J* and working point *P* for each

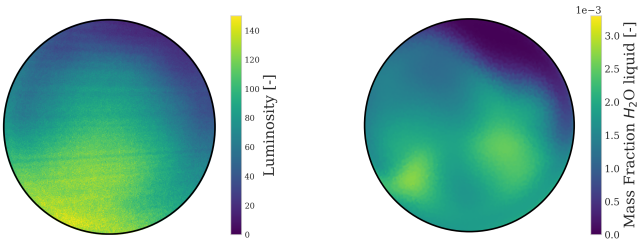

(a) Laser visualization (b) CFD simulation

Figure 21: Comparison between the luminosity on the Laser visualization (a) and the time-averaged mass fraction of condensed water predicted by the CFD URANS simulation (b) at the outlet cross section of junction B for working point P1.

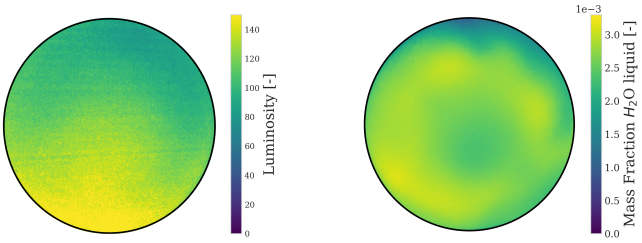

(a) Laser visualization (b) CFD simulation

Figure 22: Comparison between the luminosity on the Laser visualization (a) and the time-averaged mass fraction of condensed water predicted by the CFD URANS simulation (b) at the outlet cross section of junction B for working point P2.

technique are normalized with those of the case with higher condensation, i.e., the working point P2 with the junction B. Equations 9 and 10 show how this average and normalization are conducted:

$$\widetilde{L}_{\mathrm{J,P}} = \frac{\sum L_{\mathrm{J,P}}/N}{\sum L_{\mathrm{JB,P2}}/N} \tag{9}$$

$$\widetilde{y}_{\mathrm{cond.\ J,P}} = \frac{1/A \sum y_{\mathrm{cond.\ J,P}} \cdot dA}{1/A \sum y_{\mathrm{cond.\ JB,P2}} \cdot dA} \tag{10}$$

As a sample of the method employed for obtaining the data that will be reported in table 4, the calculations for junction B at working point P1 are described. First, luminosity is summed over all pixels and divided by this number of pixels, providing an average luminosity of $L_{\mathrm{JB,P1}} = 62.84$ (see Fig. 21a). For that point, the area-weighted average of condensed mass fraction is directly provided by StarCCM+, with a value of $y_{\mathrm{cond.\ JB,P1}} = 1.58 \cdot 10^{-3}$ (see Fig. 21b). To normalize, the same method is applied for junction B at working point P2 (maximum condensation), yielding an average luminosity of $L_{\mathrm{JB,P2}} = 91.70$ (see Fig. 22a) and an area-weighted average of liquid water mass fraction of $y_{\mathrm{cond.\ JB,P2}} = 1.90 \cdot 10^{-3}$ (see Fig. 22b). Dividing the corresponding values in accordance with Eqs. 9 and 10, one obtains the normalized values for the experiments ($\widetilde{L}_{\mathrm{JB,P1}} = 0.69$) and for the CFD simulations ($\widetilde{y}_{\mathrm{cond.\ JB,P1}} = 0.83$).

Table 4: Normalized luminosity (exp) and predicted condensation (CFD) for all the test matrix.

	Operating point	$\widetilde{L}_{\mathrm{J,P}}$ (exp)	$\widetilde{y}_{\mathrm{cond.\ J,P}}$ (CFD)
Junction A	P1	0.14	0.18
	P2	0.19	0.19
Junction B	P1	0.69	0.83
	P2	1.0	1.0

Table 4 shows the normalized luminosity for the laser visualization technique and the normalized condensation at the CFD simulations. As can be seen, the tendencies discussed in previous sections are in agreement with the quantification presented at table 4. Both junctions provide less condensation at working point P1 than at P2. Also, three-way junction A produces less condensation than junction B for both operating conditions. Even though the relationship between condensation mass fraction and luminosity is not necessarily linear, the agreement between the normalized luminosity and normalized condensation is satisfactory for the 3 remaining cases (excluding obviously the one used to normalize).

5. Potential of multiphase 3D CFD simulations for improving LP-EGR systems

An example is presented to demonstrate the potential of the 3D CFD simulations as a tool to:

- Improve the three-way junction designs to reduce as much

as possible the condensation caused by the mixing behavior, in order to mitigate compressor damage shown in the literature [12, 48].

- Increase EGR rates (see Eq. 8) up until the condensation mass flow rate is the maximum bearable for the sake of compressor durability (see the threshold case presented by Galindo et al. [14]), and in this way minimize engine pollutant emissions [3].

In this section, three-way junction A depicted in left hand side of Fig. 12 is considered as a baseline. The EGR duct diameter is increased by 25% (as can be seen in Fig. 23) to assess if this geometry modification is beneficial for condensation. A CFD simulation is therefore conducted at working point P2 (see table 3).

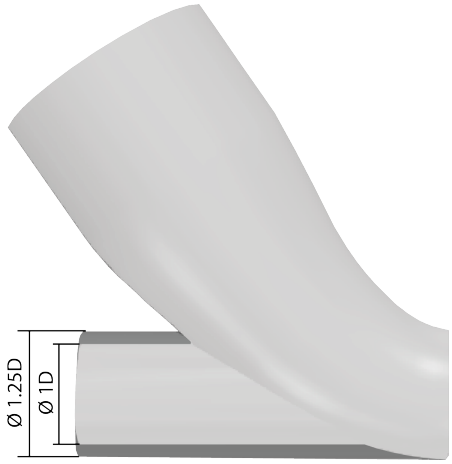

Figure 23: Increase of EGR diameter in junction A.

Considering the condensed water mass flow rate $\dot{m}_{\text{cond}}$ going through the junction outlet cross section, a value of $4.796 \cdot 10^{-2}$ kg/h is obtained for the original three-way junction A at P2. The junction with an increased EGR diameter provides a condensation of $\dot{m}_{\text{cond}} = 3.526 \cdot 10^{-2}$ kg/h instead, with a substantial reduction of 30% just by modifying the junction geometry. Contours of mass fraction of condensed water at the outlet cross section are depicted for the baseline junction A (Fig. 24a) and its counterpart with a greater EGR duct diameter (Fig. 24b). 3D CFD simulations predict that reducing the EGR velocity by increasing the EGR pipe area entails a reduction in the interface length (compare Fig. 24a and Fig. 24a), with a subsequent reduction in condensation. If the compressor was able to withstand the original condensation, an additional simulation would show that the new junction design allows to increase the EGR mass flow rate up to 50% (and EGR rate by 30%, in accordance with Eq. 8), to achieve a condensation mass flow rate of $\dot{m}_{\text{cond}} = 4.796 \cdot 10^{-2}$ kg/h again. Notice that Fig.24c presents an average condensation mass fraction lower than that of the baseline case (Fig. 24a), but its normal velocity is greater due to the increase in mass flow rate.

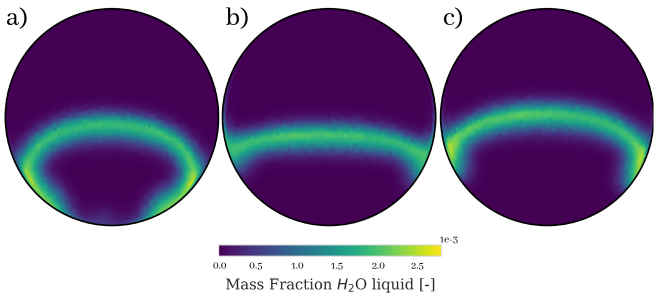

Figure 24: Comparison between the mass fraction of condensed water predicted by CFD simulations at the outlet cross section of junction A for working point P2, considering the baseline case (a), the case with a 25% increase of EGR diameter (b) and the case with a 25% increase of EGR diameter and a 50% increase of the EGR mass flow rate (c).

6. Concluding remarks

In this work, the mixing between two streams with different psychrometric conditions in a three-way junction has been addressed. The secondary flows presented at the outlet cross-section and the condensation generated in the junction have been analyzed by means of experimental techniques as well as CFD simulations.

Regarding the experimental measurements, a humid gas stand to reproduce EGR and a climatic chamber to obtain cold flow are originally combined to reproduce the flow in a LP-EGR junction. A free-discharge configuration is selected for the junction, whose impact is found to be below 3%. This configuration allows the employment of two different optical techniques to analyze the outlet transversal section of the junction. On one

hand, laser PIV measurements have been used to characterize the in-plane velocity of the cross section and to obtain the pattern of the secondary flows. On the other hand, the condensation generated due to the mixing process is studied for the first time with planar laser-induced visualization. Flow field and condensation at two different operating points at the outlet of two different junctions has been characterized, allowing a comparison of the corresponding experimental techniques with 3D-CFD simulations enhanced with a condensation submodel [13].

The proposed CFD configuration obtains a flow distribution which is generally in agreement with the experimental PIV measurements. The CFD model predicts the main flow features and how they change when considering different junctions or operating points. Considering planar laser-induced visualization and CFD condensation simulations, they both agree in showing a greater condensation for those cases with stronger secondary flows and air-EGR mixing.

Both techniques suggest that a careful design of a LP-EGR junction (if allowed by the engine packaging constraints) is able to decrease air-EGR mixing and secondary flows. Depending on the junction, the air-EGR mixing is either located at a narrow interface or is performed across the whole cross-section, which boosts the produced condensation. Indeed, a reduction of condensation mass flow rate of 5 times (for the same working point) can be found when modifying the junction geometry.

Therefore, the present work confirms the importance of the junction design to abate the condensation arriving to the compressor impeller due to LP-EGR through the reduction of secondary flows and air-EGR mixing. Optimizing the junction to minimize condensation, which can be performed with the CFD model qualitatively validated with the results shown in this work, would therefore act as a key enabler to increase the LP-EGR rates during engine warm-up and thus abate NO_x, CO_2 and particulate matter emissions. However, Guilain et al. [49] showed that geometries that reduce the condensation formation could decrease the efficiency of the compressor, so a trade-off should be obtained.

7. Acknowledgements

This work has been partially supported by "Conselleria de Innovación, Universidades, Ciencia y Sociedad Digital de la Generalitat Valenciana" through grant number GV/2020/008. Francisco Moya is partially supported through a FPI-GVA-ACIF-2019 grant of the Government of Generalitat Valenciana and the European Social Fund. The authors of this paper wish to thank Alejandro Hernández Salmerón and David González Domínguez for his invaluable support during the laboratory setup and the experimental campaign and José Vicente Pastor for his support regarding the optical techniques.

List of Symbols

c_p	isobaric specific heat capacity	$J \cdot kg^{-1} \cdot K^{-1}$
f	additional terms	–
f_L	correction factor	–
N	Number of photos	–
S	source term	
T	temperature	K
$\vec{u}$	velocity	$m \cdot s^{-1}$
w	specific humidity	$g_{H_2O} \cdot kg_{air}^{-1}$
y	mass fraction	
$\bar{Lm}$	normalized luminosity	–
Δt	characteristic time	s
MFR	Mass flow rate	$kg \cdot h^{-1}$
ρ	density	$kg \cdot m^{-3}$
σ	standard deviation	-

References

[1] T. Lu, D. Attinger, S. M. Liu, Large-eddy simulations of velocity and temperature fluctuations in hot and cold fluids mixing in a tee junction with an upstream straicht or elbow main pipe, Nuclear Engineering and Design 263 (2013) 32–41. doi:10.1016/j.nucengdes.2013.04.002.

[2] B. Yang, W. Su, S. Deng, L. Zhao, P. Lu, State-of-art of impacting T-junction: Phase separation, constituent separation and applications, International Journal of Heat and Mass Transfer 148 (2020) 1–10. doi:10.1016/j.ijheatmasstransfer.2019.119067.

[3] M. Lapuerta, A. Ramos, D. Fernandez-Rodriguez, I. Gonzalez-Garcia, High-pressure versus low-pressure exhaust gas recirculation in a Euro 6

Sub- and Superscripts

cond	condensates
corr	corrected luminosity
dryair	dry air flow
EGR	egr flow
film	laser sheet
ener.	energy
H_2O	liquid water
i	each pixel data
in	intake flow
L	Luminosity
$liquid - MFR$	liquid Mass Flow Rate
mom.	momentum
vap	water vapor

List of abbreviations

BSFC	Break specific fuel consumption
CFD	Computational fluid dynamics
EGR	Exhaust gas recirculation
LP-EGR	Low-pressure EGR
HP-EGR	High-pressure EGR
MFR	Mass flow rate
NOx	Nitrogen oxides
PIV	particle image velocimetry
RANS	Original image without postprocessing
RAW	Reynolds-Averaged Navier-Stokes
RH	Relative humidity
ROI	Region Of Interest
URANS	Unsteady Reynolds-Averaged Navier-Stokes
WLTC	Worldwide harmonized light vehicles test cycle
WLTP	Worldwide harmonized light vehicles test procedure

diesel engine with lean-NOx trap: Effectiveness to reduce NOx emission, International Journal of Engine Research - (2018) 0–9. doi:10.1177/1468087418817447.

[4] J. Galindo, H. Climent, R. Navarro, J. Miguel-García, A study on the high pressure EGR transport and application to the dispersion among cylinders in automotive engines, International Journal of Engine Research (2020). doi:10.1177/1468087420969263.

[5] J. Galindo, H. Climent, R. Navarro, G. García-Olivas, Assessment of the numerical and experimental methodology to predict egr cylinder-to-cylinder dispersion and pollutant emissions, International Journal of Engine Research (2020) 1468087420972544doi:10.1177/1468087420972544.

[6] P. Olmeda, J. Martín, F. Arnau, S. Artham, Analysis of the energy balance during World harmonized Light vehicles Test Cycle in warmed and cold conditions using a Virtual Engine, International Journal of Engine Research - (2020) 0–18. doi:10.1177/1468087419878593.

[7] K. L. Wang, D. Li, N. Husnain, S. Fareed, Numerical and experimental investigation on water vapor condensation in turbulent flue gas, Applied Thermal Engineering 160 (2019). doi:10.1016/j.applthermaleng.2019.114009.

[8] C. Guo, Q. Liu, B. Zheng, Y. You, Y. Li, Development of model based on condensation area ratio and effect on heat transfer capacity of indirect evaporative cooling, Applied Thermal Engineering 164 (2020). doi:10.1016/j.applthermaleng.2019.114557.

[9] J. Luján, V. Dolz, J. Monsalve-Serrano, M. Bernal, High-pressure exhaust gas recirculation line condensation model of an internal combustion diesel engine operating at cold conditions, International Journal of Engine Research (2019). doi:10.1177/1468087419868026.

[10] J. Galindo, V. Dolz, J. Monsalve-Serrano, M. Bernal, L. Odillart, Advantages of using a cooler bypass in the low-pressure exhaust gas recirculation line of a compression ignition diesel engine operating at cold conditions, International Journal of Engine Research (2020). doi:10.1177/1468087420914725.

[11] P. Z. John, T. Koka, S. Dayalan, Water droplet erosion simulation of a turbocharger compressor wheel, in: ASME Turbo Expo 2014: Turbine Technical Conference and Exposition, no. GT2014-26974, American Society of Mechanical Engineers, 2014.

[12] J. R. Serrano, P. Piqueras, E. Angiolini, C. Meano, J. De La Morena, On Cooler and Mixing Condensation Phenomena in the Long-Route Exhaust Gas Recirculation Line, in: SAE Technical Paper, 2015. doi:10.4271/2015-24-2521.

[13] J. Serrano, P. Piqueras, R. Navarro, D. Tarí, C. Meano, Development and verification of an in-flow water condensation model for 3D-CFD simulations of humid air streams mixing, Computers & Fluids 167 (2018) 158 – 165. doi:10.1016/j.compfluid.2018.02.032.

[14] J. Galindo, P. Piqueras, R. Navarro, D. Tarí, C. M. Meano, Validation and sensitivity analysis of an in-flow water condensation model for 3D-CFD simulations of humid air streams mixing, International Journal of Thermal Sciences 136 (2018) 410–419. doi:10.1016/j.ijthermalsci.2018.10.043.

[15] J. Galindo, R. Navarro, D. Tarí, G. García-Olivas, Centrifugal compressor influence on condensation due to Long Route-Exhaust Gas Recirculation mixing, Applied Thermal Engineering 144 (2018) 901–909. doi:10.1016/j.applthermaleng.2018.09.005.

[16] B. Yang, W. Su, S. Deng, L. Zhao, State-of-art of branching T-junction: Experiments, modeling, developing prospects and applications, Exper-

imental Thermal and Fluid Sciences 109 (2019). doi:10.1016/j.expthermflusci.2019.109895.

[17] H. Li, G. Wei, Y. Wang, D. Yang, B. Sun, W. Hong, Investigation on the phase split characteristics of slug and annular flow in a metal foam-filled T-junction, Experimental Thermal and Fluid Science 109 (109878) (2019). doi:10.1016/j.expthermflusci.2019.109878.

[18] P. Lu, S. Deng, L. Zhao, Y. Zhao, W. Xu, Y. Zhang, Analysis of pressure drop in T-junction and its effect on thermodynamic cycle efficiency, Applied Energy 231 (2018) 1–13. doi:10.1016/j.apenergy.2018.09.134.

[19] M. Zhou, R. Kulenovic, E. Laurien, Advanced flow pattern for describing tangential flow oscillation in thermal-mixing pipe flow at a horizontal T-Junction, International Journal of Thermal Sciences 136 (2019) 328–336. doi:10.1016/j.ijthermalsci.2018.10.045.

[20] M. Zhou, R. Kulenovic, E. Laurien, T-junction experiments to investigate thermal-mixing pipe flow with combined measurement techniques, Applied Thermal Engineering 150 (2019) 237–249. doi:10.1016/j.applthermaleng.2018.12.161.

[21] C. Evrim, X. Chu, E. Laurien, Analysis of thermal mixing characteristics in different T-junction configurations, International Journal of Heat and Mass Transfer 158 (2020) 1–10. doi:10.1016/j.ijheatmasstransfer.2020.120019.

[22] M. Georgiou, M. V. Papalexandris, Turbulent mixing in T-junctions: The role of the temperature as an active scalar, International Journal of Heat and Mass Transfer 115 (2017) 793–809. doi:10.1016/j.ijheatmasstransfer.2017.08.081.

[23] A. Reihani, J. Hoard, S. Klinkert, C. Kuan, D. Styles, Experimental response surface study of the effects of low-pressure exhaust gas recirculation mixing on turbocharger compressor performance, Applied Energy 261 (2020) 1–16. doi:10.1016/j.apenergy.2019.114349.

[24] A. Sakowitz, M. Mihaescu, L. Fuchs, Turbulent flow mechanisms in mixing T-junctions by Large Eddy Simulations, International Journal of Heat and Fluid Flow 45 (2014) 135–146. doi:10.1016/j.ijheatfluidflow.2013.06.014.

[25] T. Xue, S. Zhang, Investigation on heat transfer characteristics of falling liquid film by planar laser-induced fluorescence, International Journal of Heat and Mass Transfer 126 (2018) 715–724. doi:10.1016/j.ijheatmasstransfer.2018.05.039.

[26] C. Brucker, Study of the three-dimensional flow in a T-junction using a dual-scanning method for three-dimensional scanning-particle-image velocimetry (3-D SPIV), Experimental Thermal and Fluid Science 14 (1) (1997) 35–44. doi:10.1016/S0894-1777(96)00110-0.

[27] C. Espinoza, M. Simmons, F. Alberini, O. Mihailova, D. Rothman, A. Kowalski, Flow studies in an in-line Silverson 150/250 high shear mixer using PIV, Chemical Engineering Research and Design 132 (2018) 989–1004. doi:10.1016/j.cherd.2018.01.028.

[28] L. Chen, X. Zhang, C. Wang, C. Yang, Analysis on High-Pressure Water Separator, Procedia Engineering 121 (2015) 558–566. doi:10.1016/j.proeng.2015.08.1034.

[29] CD-adapco, STAR-CCM+, release version 12.06.010 Edition (February 2018).
URL http://ww.cd-adapco.com

[30] J. Galindo, R. Navarro, D. Tari, F. Moya, Development of an experimental test bench and a psychrometric model for assessing condensation on a Low Pressure EGR cooler, International Journal of Engine Research 22 (2020) 1540–1550. doi:10.1177/1468087420909735.

[31] A.J.Torregrosa, A.Broatch, J.V.Pastor, J.García-Tíscar, Measuring turbocharger compressor inlet backflow through particle image velocimetry, Experimental Thermal and Fluid Science 99 (2018) 420–432. doi:10.1016/j.expthermflusci.2018.08.015.

[32] J. V. Pastor, J. M. García-Oliver, A. García, M. Pinotti, Effect of laser induced plasma ignition timing and location on Diesel spray combustion, Energy Conversion and Management 133 (2017) 41–55. doi:10.1016/j.enconman.2016.11.054.

[33] A. Sciacchitano, B. Wieneke, PIV uncertainty propagation, Measurement Science and Technology 27 (2016) 1–16. doi:10.1088/0957-0233/27/8/084006.

[34] L. Pickett, C. Genzale, J. Manin, L.-M. Malbec, Measurement Uncertainty of Liquid Penetration in Evaporating Diesel Sprays, in: 23^{rd} Annual Conference on Liquid Atomization and Spray Systems, ILASS Americas, 2011.

[35] J. V. Pastor, J. J. Lopez, J. E. Julia, J. V. Benajes, Planar Laser-Induced Fluorescence fuel concentration measurements in isothermal Diesel sparys, Optics Express 10 (2002) 309–323. doi:10.1364/OE.10.000309.

[36] A. Charogiannis, J. Sik, V. Voulgaropoulos, C. Markides, Structured planar laser-induced fluorescence (S-PLIF) for the accurate identification of interfaces in multiphase flows, International Journal of Multiphase Flow 118 (2019) 193–204. doi:10.1016/j.ijmultiphaseflow.2019.06.002.

[37] D. C. Wilcox, Reassessment of the scale-determining equation for advanced turbulence models, AIAA journal 26 (11) (1988) 1299–1310. doi:10.2514/3.10041.

[38] D. Tarí, Effect of inlet configuration on the performance and durability of an automotive turbocharger compressor, Ph.D. thesis, Universitat Politècnica de València. Departamento de Máquinas y Motores Térmicos (June 2018). doi:10.4995/Thesis/10251/104410.
URL http://hdl.handle.net/10251/104410

[39] S. Schuster, D. Brillert, F. Benra, Condensation in Radial Turbines-Part I: Mathematical Modeling, Journal of Turbomachinery 140 (2018) 1–9. doi:10.1115/1.4040934.

[40] S. Schuster, D. Brillert, F. Benra, Condensation in Radial Turbines-Part II: Application of the Mathematical Model to a Radial Turbine Series, Journal of Turbomachinary 140 (2018) 1–7. doi:10.1115/1.4040935.

[41] T. Wittmann, C. Bode, J. Friedrichs, The Feasibility of an Euler-Lagrange Approach for the Modeling of Wet Steam, Journal of Engineering for gas

turbines and power 143 (2021) 1–8. doi:10.1115/1.4049859.

[42] T. Wittman, S. Luck, C. Bode, J. Friedrichs, Numerical Simulation of Nucleation and Condensation and Radial Turbines, in: CAD-FEM ANSYS Simulation Conference, Dusseldorf, Germany, 2019.

[43] K. Sakakura, S. Yamamoto, Numerical and experimental predictions of heterogeneous condensate flow of moist air in cooled pipe, International Journal of Heat and Fluid Flow 27 (2006) 220–228. doi:10.1016/j.ijheatfluidflow.2005.08.006.

[44] R. Tunstall, D. Laurence, R. Prosser, A. Skillen, Large eddy simulation of a T-Junction with upstream elbow: The role of Dean vortices in thermal fatigue, Applied Thermal Engineering 107 (2016) 672–680. doi:10.1016/j.applthermaleng.2016.07.011.

[45] E. Idelchik, E. Fried, Handbook of hydraulic resistance, Jaico Publishing House, 1986.

[46] Y. Xue, R. Hhellmuth, D. Shin, Formation of Vortices in Idealised Branching Vessels: A CFD Benchmark Study, Cardiovascular Engineering and Technology 11 (2020) 544–559. doi:10.1007/s13239-020-00477-9.

[47] W. H. Lyne, Unsteady viscous flow in a curved pipe, Journal of Fluid Mechanics 45 (1) (1971) 13–31. doi:10.1017/S0022112071002970.

[48] S. Karstadt, J. Werner, S. Münz, R. Aymanns, Effect of water droplets caused by low pressure egr on spinning compressor wheels, in: Aufladetechnische Konferenz, Dresden, 2014.

[49] S. Guilain, R. Boubennec, M. Doublet, C. Clement, R. Navarro, D. Tarí, F. Moya, Condensation before compressor: a key issue of Low Pressure EGR in Eu7 context, in: 24th Supercharging Conference 2019, Aufladetechnische Konferenz, Dresden, 2019.